BIOCHEMISTRY
including biophysical chemistry & molecular biology

Article

pubs.acs.org/biochemistry

Femtosecond Photodynamics of the Red/Green Cyanobacteriochrome NpR6012g4 from *Nostoc punctiforme*. 2. Reverse Dynamics

Peter W. Kim,[†] Lucy H. Freer,[†] Nathan C. Rockwell,[‡] Shelley S. Martin,[‡] J. Clark Lagarias,[‡] and Delmar S. Larsen*,[†]

[†]Department of Chemistry and [‡]Department of Molecular and Cell Biology, University of California, One Shields Avenue, Davis, California 95616, United States

Supporting Information

ABSTRACT: Phytochromes are red/far-red photosensory proteins that utilize photoisomerization of a linear tetrapyrrole (bilin) chromophore to photoconvert reversibly between red- and far-red-absorbing forms (P_r and P_{fr}, respectively). Cyanobacteriochromes (CBCRs) are related photosensory proteins with more diverse spectral sensitivity. The mechanisms that underlie this spectral diversity have not yet been fully elucidated. One of the main CBCR subfamilies photoconverts between a red-absorbing 15*Z* ground state, like the familiar P_r state of phytochromes, and a green-absorbing photoproduct ($^{15E}P_g$). We have previously used the red/green CBCR NpR6012g4 from the cyanobacterium *Nostoc punctiforme* to examine ultrafast photodynamics of the forward photoreaction. Here, we examine the reverse reaction. Using excitation-interleaved transient absorption spectroscopy with broadband detection and multicomponent global analysis, we observed multiphasic excited-state dynamics. Interleaved excitation allowed us to identify wavelength-dependent shifts in the ground-state bleach that equilibrated on a 200 ps time scale, indicating ground-state heterogeneity. Compared to the previously studied forward reaction, the reverse reaction has much faster excited-state decay time constants and significantly higher photoproduct yield. This work thus demonstrates striking differences between the forward and reverse reactions of NpR6012g4 and provides clear evidence of ground-state heterogeneity in the phytochrome superfamily.

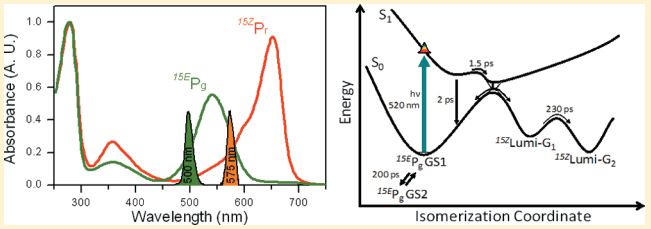

Photosensory proteins such as phytochromes play important roles in the photobiology of both photosynthetic and nonphotosynthetic organisms.[1−5] Canonical phytochromes utilize linear tetrapyrrole (bilin) chromophores to photoconvert between red-absorbing P_r and far-red-absorbing P_{fr} states, with primary photochemistry generally thought to occur at the 15,16 double bond.[6−8] The bilin chromophore is bound within a conserved pocket on a GAF (cGMP phosphodiesterase/adenylyl cyclase/FhlA) domain that is part of a conserved photochemical core module consisting of PAS, GAF, and PHY domains.[1,9−14] Cyanobacteriochromes (CBCRs) make up a recently discovered class of related photoreceptors that require only the GAF domain itself to assemble with the chromophore and undergo photoconversion. CBCRs utilize phycocyanobilin (PCB) as a chromophore precursor and exist in several subfamilies with considerable variation in their spectral photosensory activity.[15−28] Members of one of the main subfamilies, the red/green CBCRs, exhibit a red-absorbing 15*Z* ground state [$^{15Z}P_r$ (Figure 1A)] and reversibly photoconvert to a green-absorbing 15*E* photoproduct ($^{15E}P_g$), which can thermally revert to P_r over time.[20,22,24,25] We have used NpR6012g4, a functional red/green CBCR encoded within the *NpR6012* locus of the cyanobacterium *Nostoc punctiforme* ATCC 2913, to conduct the first study of primary photochemistry in any CBCR (DOI: 10.1021/bi201507k and ref 29).

These studies used ultrafast transient absorption pump−probe (PP) and pump−dump−probe experiments in combination with broadband detection and global data analysis[30−39] to probe the primary photodynamics of the NpR6012g4 forward reaction ($^{15Z}P_r \rightarrow {}^{15E}P_g$). Decay kinetics for the excited state and the absorbance spectrum of the Lumi-R primary photoproduct were similar to those observed for the red/far-red phytochrome Cph1. However, an unusually high (40%) quantum yield for photoconversion (Φ) was observed for NpR6012g4, well above those reported for canonical phytochrome systems (∼15%). Broadband pump−dump−probe (PDP) spectroscopy demonstrated that this high Φ value arises from formation of Lumi-R from both the excited-state population and a productive ground-state intermediate.[29] Therefore, despite a conserved mechanism of photoconversion, an identical bilin chromophore, and similar spectral evolution, the phytochrome Cph1 and CBCR NpR6012g4 exhibit distinct photodynamics.

In this work, we examine the femtosecond dynamics of the reverse photoreaction ($^{15E}P_g \rightarrow {}^{15Z}P_r$). While this reaction is quite different from the reverse reaction of Cph1 because of the

Received: November 22, 2011
Revised: December 9, 2011
Published: December 12, 2011

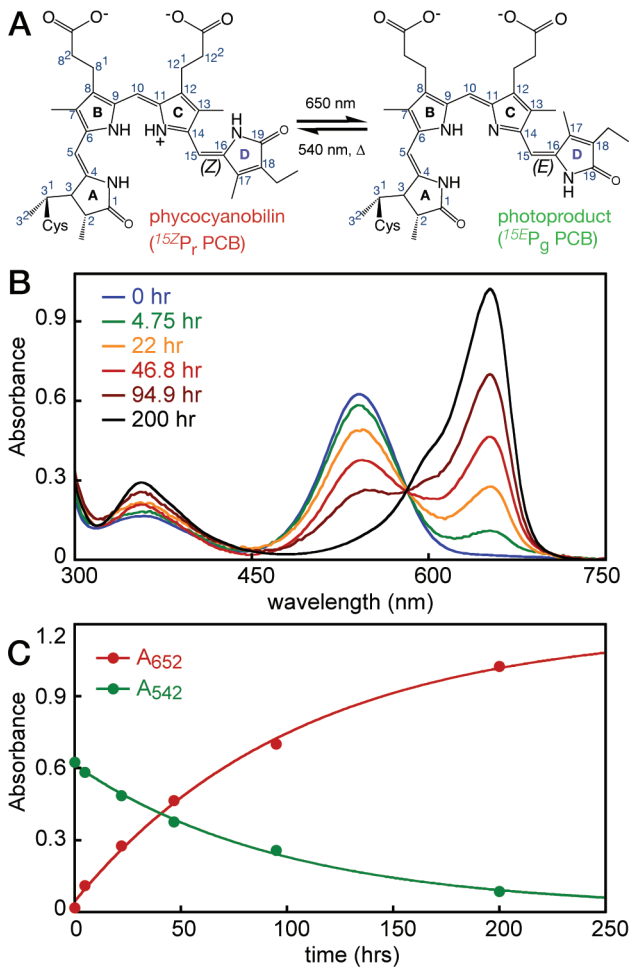

Figure 1. Reverse reaction of NpR6012g4. (A) Proposed photostates of the red/green CBCR NpR6012g4. The phycocyanobilin chromophore is thought to be protonated in the red-absorbing $^{15Z}P_r$ state (left) but deprotonated in the green-absorbing $^{15E}P_g$ state (right). (B) Thermal stability of the $^{15E}P_g$ photoproduct assessed by prolonged incubation in darkness at room temperature. Aliquots were withdrawn and characterized by absorption spectroscopy at the indicated times. (C) Absorbance was plotted as a function of time at selected wavelengths from the data set shown in panel B. Data were fit to single-exponential progress curves, giving a dark reversion rate of 0.01 h^{-1} ± 10%.

different photoproducts, flash photolysis studies of a related red/green CBCR, AnPixJg2,[25] have demonstrated formation of a red-shifted primary photoproduct $G1_{570}$ at or before the 50 ns probe time. We have now measured the formation of the equivalent product in NpR6012g4 on a picosecond time scale with complicated excited-state dynamics. Ground-state heterogeneity was also demonstrated for the reverse reaction via an interleaved PP setup in which the two PP signals were measured on the same sample to address excitation dependence.[40] The real-time collection of two separate PP signals with different excitation wavelengths afforded identical experimental conditions and allowed observation of subpopulations with different absorption bands in fast equilibrium. The primary photoconversion efficiency was also wavelength-dependent but was very high (~50%). This work thus provides new insight into the photochemical behavior of red/green CBCRs and other members of the greater phytochrome superfamily.

MATERIALS AND METHODS

Protein Preparation and Static Measurements. Purification of NpR6012g4 as an intein−chitin binding domain (intein−CBD) fusion was performed as described in the preceding paper (DOI: 10.1021/bi201507k). After lysis, ultracentrifugation, and binding to chitin resin (NEB) in accordance with the manufacturer's instructions, intein cleavage was initiated by addition of DTT to the column, followed by overnight incubation at 4 °C. Peak fractions were pooled and dialyzed against TKKG buffer [25 mM TES-KOH (pH 7.8), 100 mM KCl, and 10% (v/v) glycerol] overnight prior to being frozen in liquid nitrogen and stored at −80 °C.

To ensure adequate stability of the photoproduct in the flow path of the sample for collection of transient signals (see the next section), dark reversion experiments were performed. NpR6012g4 was photoconverted to $^{15E}P_g$ by illumination with 650 ± 20 nm light, and the sample was then incubated at room temperature in darkness. Aliquots were removed over a 200 h period and examined by absorbance spectroscopy using a Cary 50 instrument (Figure 1B). Absorbance values at selected wavelengths characteristic of the two photostates were plotted as a function of time and fit to single-exponential progress curves (Figure 1C), giving an apparent rate constant for dark reversion of 0.01 h^{-1} ± 10%.

Transient Signals. The dispersed-probe transient absorption setup was constructed from an amplified Ti:sapphire laser system (Spectra Physics Spitfire Pro + Tsunami) operating at 1 kHz, which produced 2.25 mJ pulses of 800 nm fundamental output with a 40 fs (full width at half-maximum) duration.[41] The 800 nm fundamental pulse train from the amplifier was split into multiple paths. One path generated the dispersed white light probe supercontinuum (440−750 nm) by focusing the laser pulses into a slowly translating CaF_2 crystal. The white light probe beam was measured with a 256 pixel photodiode array (Hamamatsu C7884E) after diffraction by grating for simultaneous broadband measurements. Two other paths were used to generate tunable visible pulses from a pair of independently operating home-built noncollinear optical parametric amplifiers (NOPAs), providing two excitation/pump sources for examining the wavelength dependence of the reverse reaction dynamics. In this interleaved pump−probe setup, the 500 and 575 nm excitation pulses that were generated from the NOPAs were impinged and overlapped, both spectrally and temporally, on the NpR6012g4 sample (Figure 2). The 500 and 575 nm pump

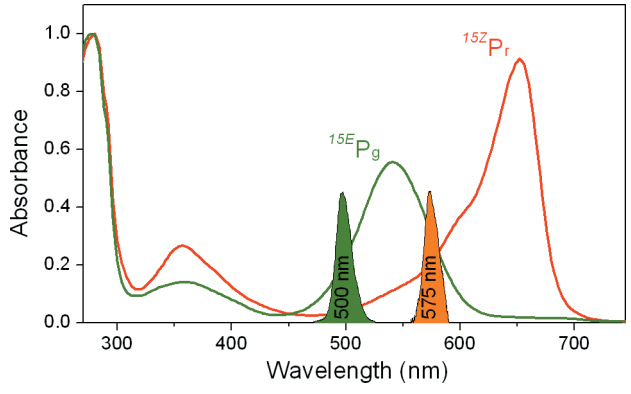

Figure 2. Interleaved PP initiation of the reverse reaction of NpR6012g4. The $^{15E}P_g$ ground-state absorbance (solid green line) is shown overlaid with spectra of the 500 nm (green fill) and 575 nm (orange fill) pulses used for interleaved PP measurements. The P_r ground-state absorbance (solid red line) is plotted for reference.

dx.doi.org/10.1021/bi2017365 | Biochemistry 2012, 51, 619−630

beams were optically chopped at 500 and 250 Hz, respectively, to generate a pulse sequence in which the reference spectrum and excited spectra were collected sequentially. The interleaved pump−probe approach minimizes errors caused by long-term fluctuations in excitation power, sample degradation, and different experimental conditions.[40]

The probe pulses were optically delayed with respect to the pump pulses by a computer-controlled linear-motor stage (Newport IMS 6001), which allowed up to 7 ns temporal separation. A total of 141 transient spectra from −100 ps (for pre-time zero signal correction) to 6.3 ns were collected. The pump pulses were linearly polarized at 54.7° (magic angle) with respect to the probe pulses. The ∼300 μm pump pulse and 50 μm probe pulse spot diameters were estimated using a micrometer stage and razor blade. The appreciably greater pump pulse minimizes the contributions of artifacts to the signals from a varying spatial overlap between pump and probe beams. This was confirmed by monitoring the signal amplitude and spectral shape when spatially dithering the pump beam with respect to the probe beam. The uniform decay of the transient spectrum when spatially dithering the pump and probe beam overlap (not shown) indicates that the waist of the probe beam is small compared to the pump waist and is unaffected by the Gaussian power dependency of the pump beam.

A 130 fs temporal resolution of the experiment was estimated by the rise time of the excited-state absorption bands for both excitation wavelengths. The sample was flowed continuously in a closed circuit at an estimated rate of 400 μL/s to ensure fresh sample for each excitation pulse. Before the protein entered into the cuvette, it was continuously illuminated with 2 mW of 660 nm LED light (Epitex Inc., model L660-66-60) through a quartz window to cycle the proteins to the desired $^{15E}P_g$ state for interrogation. After each experiment, the sample's absorbance spectrum was measured to check the extent of sample degradation; typically, between 10 and 20% of the protein was precipitated in each experiment, and that was also indicated by the increment of pump scatter and noise during data collection. The path length of the quartz cuvette was 2 mm, and the optical density at the visible absorption peak was 0.3−0.4 at a 2 mm path length. All the experiments were conducted at room temperature (23 °C).

RESULTS

Primary Reverse Reaction Dynamics ($^{15E}P_g \rightarrow {}^{15Z}P_r$). Excitation of the $^{15E}P_g$ population at 500 and 575 nm generated qualitatively similar PP signals (Figure 3). Both data sets exhibit clear separation of the bleach (∼550 nm) and stimulated emission (SE, ∼625 nm) bands at 700 fs and 2 ps (Figure 3). The SE band and a broad excited-state absorption (ESA) band (475 nm) are indicators of a P_g* population on the electronic excited-state surface. Both of these features decay to zero within 50 ps (Figure 4), considerably faster than that observed for the forward photodynamics of NpR6012g4 (DOI: 10.1021/bi201507k). Also in contrast to the forward P_r photodynamics (DOI: 10.1021/bi201507k), two distinct photoproducts are observed in the reverse reaction data sets: Lumi-G_1 and Lumi-G_2. The Lumi-G_1 primary photoproduct (Figure 3, 50 ps curves) evolves to the narrower, blue-shifted Lumi-G_2 (135 cm^{-1} blue shift) within 1 ns (Figure 3). Examination of kinetic traces at 620 nm for both data sets confirms Lumi-G_1 to Lumi-G_2 evolution (Figure 4).

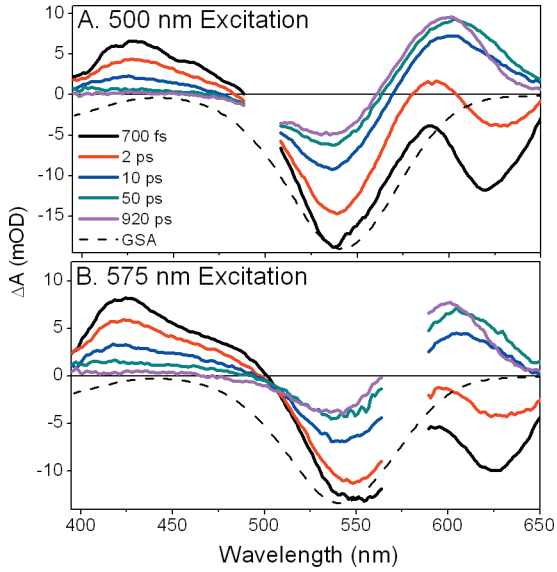

Figure 3. Transient signals from the interleaved PP experiment at selected probe times. $^{15E}P_g$ NpR6102g4 was excited at 500 (A) and 575 nm (B) at the probe times indicated in panel A. Spectra are overlaid with the inverted $^{15E}P_g$ ground-state absorbance (dashed lines).

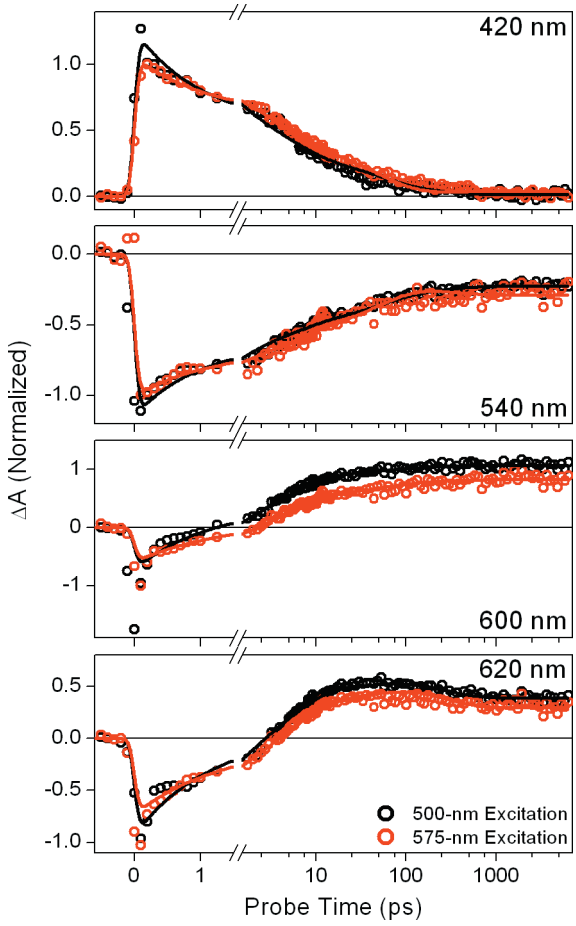

Figure 4. Kinetic traces from interleaved PP measurements at selected probe wavelengths. Normalized kinetic traces (circles) are shown for excitation at 500 (black) and 575 nm (red). Probe wavelengths are indicated in the inset. Fits (solid lines) are from the target model in Figure 7, which does not attempt to fit the initial (<500 fs) artifactual signals, unlike five-component sequential fitting (Figure S3 of the Supporting Information).

dx.doi.org/10.1021/bi2017365 | Biochemistry 2012, 51, 619−630

Although the 500 and 575 nm excitation data sets are qualitatively similar, several important differences exist. In particular, the decay of the P_g* signal is distinctly faster in the 500 nm excitation data set. This is demonstrated by the complete loss of the ESA band by 50 ps upon 500 nm excitation, but the persistence of the same feature at the same time after 575 nm excitation (Figure 3, cyan curves). Kinetic traces normalized at the initial amplitude of the signals at different probe wavelengths exhibit consistently faster kinetics before ~20 ps upon 500 nm excitation (Figure 4). Furthermore, the photochemical quantum yield Φ is also dependent on the excitation wavelength, with the faster 500 nm excitation data set exhibiting an ~15% higher quantum yield as indicated by the relative amplitude of the Lumi-G_2 population versus the initial P_g* population (Figure 4, 600 nm probe).

The spectral features of the signals are also affected by the excitation wavelength. The 700 and 2 ps spectra (Figure 3, black and red curves) after 500 nm excitation exhibit a blue-shifted bleach (minimum at 540 nm) compared to that with 575 nm excitation (550 nm). A similar, but smaller, blue shift of the SE is also observed (620 and 625 nm for 500 and 575 nm excitation, respectively). Interestingly, the excitation wavelength-dependent blue shift of the bleach is dynamic and decreases over time (Figure 5): by 1 ns this effect is absent, and the Lumi-G_2 spectra overlap. It is important to note that the shifts in the bleach band indicate that the ground-state depletions are induced by the two pump wavelengths is not equivalent. Hence, there must be at least two spectrally distinct ground-state subpopulations coexisting within the $^{15E}P_g$ ground-state absorption (GSA). The loss of the wavelength-dependent bleach effects at longer times (Figure 5)

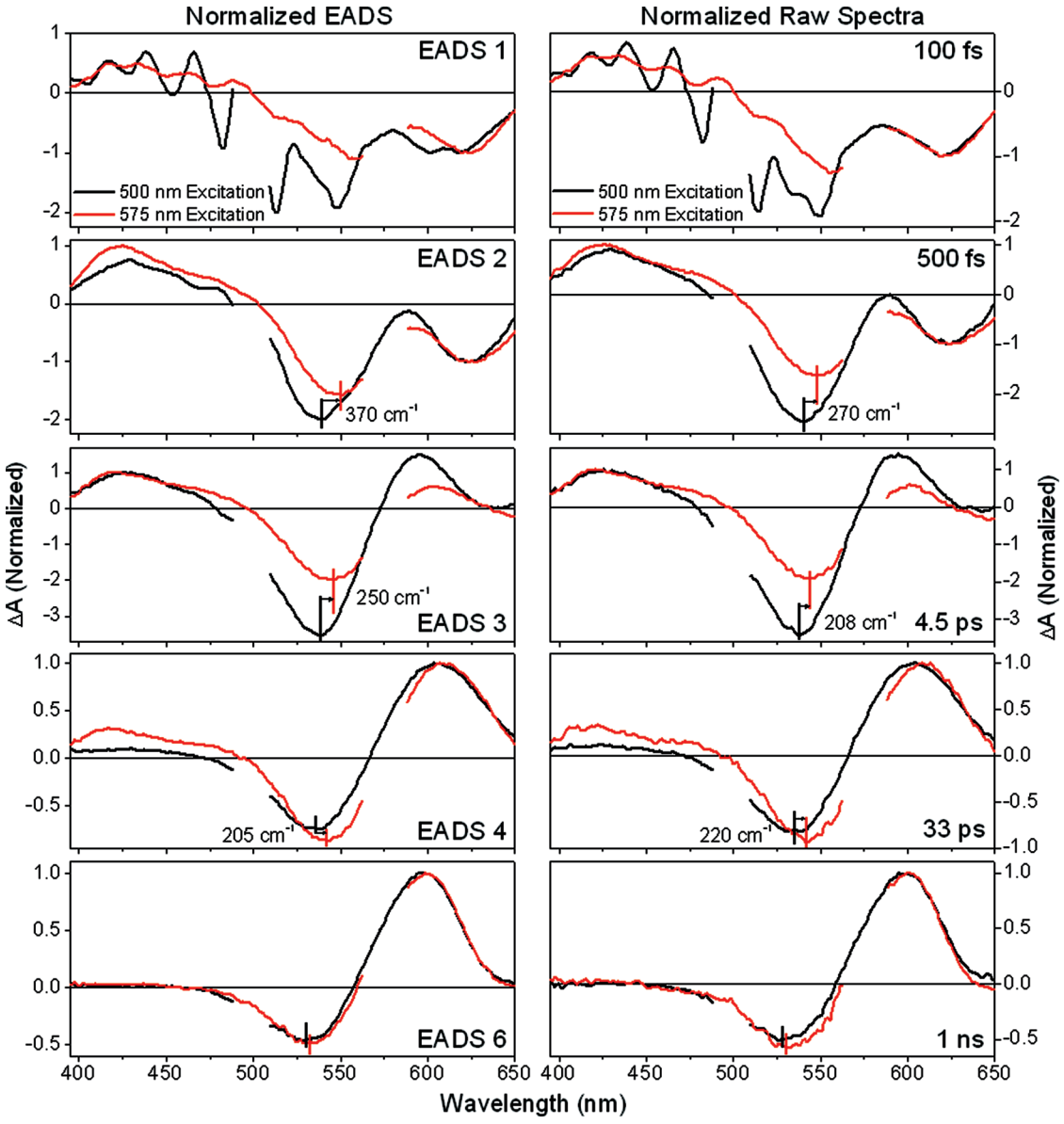

Figure 5. Sequential analysis of interleaved PP data. The left column shows EADS for interleaved PP data upon excitation at 500 (black) and 575 nm (red). EADS1 and EADS2 are normalized at the SE band (~620 nm). EADS3 is normalized at the 425 nm ESA band. EADS4 and EADS5 are normalized at the 600 nm photoproduct region. In the right column, raw transient spectra were normalized at the same regions at probe times corresponding to the EADS in the left panel. For EADS2–EADS4, minima of the bleach band are indicated for each excitation wavelength for comparison of the difference between the two bleach bands, with the corresponding energy gap indicated in wavenumbers.

dx.doi.org/10.1021/bi2017365 | *Biochemistry* 2012, 51, 619–630

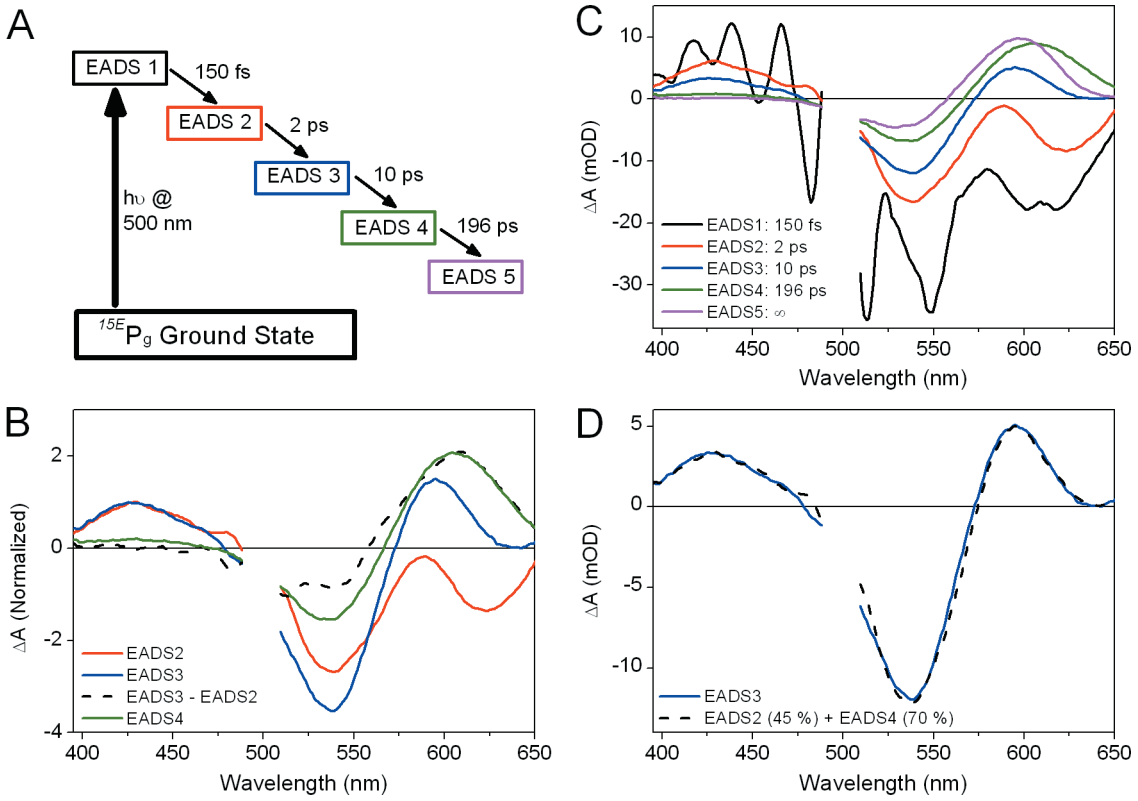

Figure 6. Sequential analysis of 500 nm excitation with a five-component sequential model. (A) Schematic of the sequential model with associated time constants. Color codes apply to all panels. (B) EADS for the five components. (C) Comparison of EADS2 and EADS3 normalized at the ESA band (420 nm). Subtraction of the normalized EADS2 from EADS3 (dashed) allows extraction of ground-state spectral evolution independent of excited-state decay. EADS4 (comparable to Lumi-G_1) is overlaid for comparison with the EADS3 minus EADS2 difference spectrum. (D) Decomposition of EADS3 using a linear combination of EADS2 and EADS4 shows that EADS3 consists of 70% of EADS4. This indicates significant formation of Lumi-G_1 by EADS3. Coefficients for the linear combination do not add to unity because of the normalization on the excited-state band.

demonstrates that those populations interconvert on a subnanosecond time scale (Figure 2). We next used this information to construct a fully inhomogeneous target model that fits both excitation wavelength data.

Global Analysis. As with the forward dynamics of NpR6012g4 (DOI: 10.1021/bi201507k), the data sets were analyzed within the global analysis formalism.[30,31] Global analysis fits all data to a postulated multipopulation "target" model to estimate the constituent populations' concentration profiles (rise and decay) in time and their respective time-independent species-associated difference spectra (SADS). The chosen target model dictates a system of linear differential equations, and those equations are numerically solved to give the best fit to the data. The final model used for interpreting the observed data was developed via an initial sequential analysis with subsequent improvements, subject to several criteria discussed below.

In the initial sequential analysis, multiple sequential states are used to fit the full data set and estimate the underlying "apparent" (i.e., directly observed) time scales in the data. This analysis generates evolution-associated difference spectra (EADS), which are the averaged spectral signatures of states with increasing lifetimes (Figure 6A). Although this "sequential EADS" approach describes the data, it does not decompose these apparent time scales into the microscopic rate constants describing the evolution of microscopic populations evolving into another.[30,31] This requires a more sophisticated "target analysis".[30,31] However, the sequential EADS are useful in extracting the spectral evolution of the reaction and its apparent time scales and in the construction of target models via the simple manipulation of the extracted EADS. We also considered a parallel decay-associated difference spectra (DADS) approach as an alternative to the sequential EADS approach (Figure S1 of the Supporting Information). This approach describes the data in a parallel model in which each DADS component decays on an apparent time scale.[30−32,42] Both approaches give comparable results and fits to the data, including a marked dependence on excitation wavelength. We prefer the sequential EADS approach, because it closely mirrors the target model analysis in the following section.

Sequential Analysis. Sequential EADS for both the 500 and 575 nm excitation of $^{15E}P_g$ were independently analyzed (Figure 6 and Figure S2 of the Supporting Information for 500 and 575 nm data, respectively). Both data sets require five compartments for an adequate fit, especially for fitting the earliest sub-500 fs signals (Figure S3 of the Supporting Information; four- and three-component sequential models not shown). Because the early time data contain significant contributions from fast artifacts such as cross-phase modulation, stimulated Raman, and two-photon absorption,[34,43−45] which generate oscillatory signals that overlap the transient absorption spectrum and which are also observed in the raw data (Figures 5 and 6B), the fastest EADS1 was incorporated to fit those artifactual signals. Subsequent EADS (i.e., EADS2−EADS5) represent the actual signals from the photoreaction. Because EADS1 confirmed that the earliest signals were oscillatory artifacts, no effort was taken to fit sub-500 fs signals in the target model analysis described below. EADS of the sequential

dx.doi.org/10.1021/bi2017365 | Biochemistry 2012, 51, 619−630

model for 500 nm excitation data are shown in Figure 6B and evolve with the following time constants: 150 fs (artifacts), 2 ps, 10 ps, 196 ps, and ∞ (photoproduct). EADS3 and EADS4 represent almost completely Lumi-G_1 and Lumi-G_2 populations, respectively, for 500 nm excitation data; thus, its slower 196 ps transition represents ground-state evolution of the primary Lumi-G photoproducts.

EADS2 is qualitatively similar to the 700 fs transient spectrum (Figure 3A), with flanking SE and ESA bands on the red and blue sides of the bleach, respectively. As expected from the raw spectra (Figure 5), the bleach band is dependent on the excitation wavelength, with a ~370 cm^{-1} shift of the bleach peak (Figure 6, EADS2). Furthermore, this spectral shift between two excitation data sets is dynamic, with the differences in the EADS3 and EADS4 bleaches differing by only 250 cm^{-1} and the final EADS5 almost completely overlapping (Figure 6).

To extract the ground-state spectral evolution independent of excited-state decay in an unbiased manner, the EADS for the 500 nm excitation data were normalized and subtracted in sequence (Figure 6C). EADS1 was omitted in this analysis because of the artifactual signals discussed above. The EADS3 minus EADS2 difference spectrum is nearly identical to EADS4, which we had previously assigned to formation of Lumi-G_1. Therefore, part of the Lumi-G_1 population is generated from the 2 ps evolution of EADS2 to EADS3. This is distinctly different from the forward reaction of $^{15Z}P_r$ NpR6012g4, in which the fastest 5 ps component fails to generate the Lumi-R photoproduct (DOI: 10.1021/bi201507k).

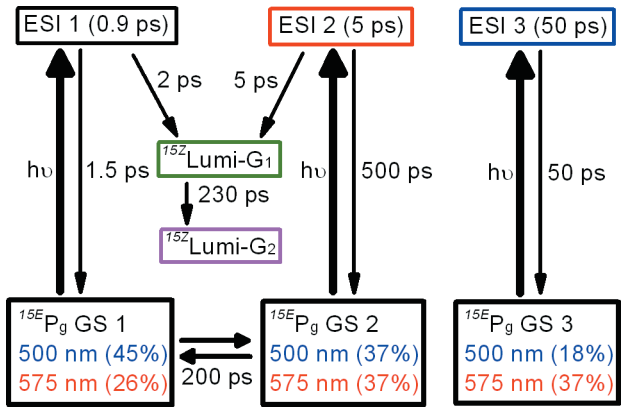

Figure 7. Global target analysis of the reverse reaction. This model includes three heterogeneous $^{15E}P_g$ ground states, with the percentage of the excited population upon 500 nm (blue) or 575 nm excitation (red) indicated in parentheses. ESI3, which decays at 50 ps, does not generate Lumi-G_1, while both ESI1 and ESI2 are productive. Time constants are indicated. Detailed parameters for calculation of the photocycle are listed in Table 1.

A comparable evaluation of the EADS4 minus EADS3 difference spectrum was inconclusive (not shown), but target analysis shows that this slower decay of P_g* does not produce Lumi-G_1 (see below). EADS3 was decomposed to extract the Lumi-G_1 contribution in EADS3 and was estimated to be 70% of the EADS4 (Lumi-G_1) amplitude. Sequential EADS analysis of the 575 nm excitation data set yielded comparable results with slightly different time scales and EADS (Figure S2 of the Supporting Information).

Target Analysis. The kinetic model that was adopted to fit and interpret both excitation wavelength-dependent data sets is shown in Figure 7 with parameters listed in Table 1. In the construction of this model, several constraints were implemented to ensure that the model is capable of simultaneously describing both excitation wavelength data sets within a physical picture.

(1) The sequential EADS analysis (Figure 6) suggested that the ESA bands exhibit nearly identical spectral properties (including extinction magnitudes or amplitudes). We therefore constrain the P_g* excited-state intermediates (ESI) to have identical SADS for each excitation wavelength data set. These constraints are not imposed on the SADS between the different data sets.

(2) The Lumi-G_1 and Lumi-G_2 SADS must exclude the SE and ESA marker bands characteristic of P_g*. This is especially important for the more slowly evolving EADS4 kinetics in the 575 nm excitation data, which contains a significant amount of long-living excited-state population overlapping the Lumi-G_1 population (Figure S2B of the Supporting Information).

(3) The Lumi-G_1 and Lumi-G_2 SADS for both data sets are expected (but not enforced) to be spectrally identical to each other for each dataset as indicated from the sequential EADS analysis data (Figure 6). The differences in populations are then represented only in the corresponding concentration profiles.

(4) The observed heterogeneity of the ground-state bleach led us to model both data sets not as two independent data sets with excitation wavelength-dependent time scales but as excitation-dependent occupations of different populations with excitation wavelength-independent kinetics (i.e., an inhomogeneous model). Of course, this would not arise from the actual dependence of the ground-state population distribution on the excitation wavelength but rather reflects wavelength-dependent contributions of the ground-state populations, implying at least slight differences in the GSA of the different populations.

(5) The failure to observe clear Lumi-G_1 formation during evolution from EADS3 to EADS4 was interpreted to indicate the presence of a third P_g* population (ESI 3) that made little to no contribution to Lumi-G_1 formation.

As already noted, Φ is dependent on excitation wavelength. The normalized 600 and 620 nm kinetic traces in Figure 4 demonstrate that the photoproduct amplitude for the 500 nm

Table 1. Interleaved Global Analysis Parameters

	ESI1	ESI2	ESI3	Lumi-G_1	Lumi-G_2
initial occupancy (500 nm)	45%	37%	18%	0%	0%
initial occupancy (575 nm)	26%	37%	37%	0%	0%
$\tau_{effective}$	0.9 ps	5 ps	50 ps	230 ps	∞
τ	1.5 ps (GS1)	500 ps (GS2)	50 ps (GS3)	230 ps (Lumi-G_2)	
	2 ps (Lumi-G_1)	5 ps (Lumi-G_1)			
branching yield	57% (GS1)	1% (GS2)	100% (GS3)	100% (Lumi-G_2)	
	43% (Lumi-G_1)	99% (Lumi-G_1)			
Lumi-G_1 yield (500 nm)	19%	37%	0%		
Lumi-G_1 yield (575 nm)	11%	37%	0%		

dx.doi.org/10.1021/bi2017365 | *Biochemistry* 2012, 51, 619–630

excitation data is 15−20% greater. Given the fact that the sample is identical in the interleaved experiment and that the only difference in the data sets is the pump wavelength, the quantum yields suggest that 500 nm light excites the productive GS population or populations more selectively. Additionally, 500 nm excitation results in faster excited-state kinetics (Figure 4, 420 nm). Hence, the proposed inhomogeneous model (Figure 7) changes the contribution of each ground-state population (GS) to the observed excited-state ensemble based on excitation wavelength, such that 500 nm light selectively excites the faster decaying GS1 subpopulation (45% vs 26%) and, conversely, 575 nm light selectively excites the slower and nonproductive GS3 subpopulation (37% vs 18%).

The target model thus contains three ground-state populations, with each producing its own ESI (Figure 7). The estimated concentration profiles and SADS for each excitation wavelength are contrasted in Figure 8. As indicated by the normalized kinetic traces at 600 and 620 nm (Figure 4), the Φ of Lumi-G_2 (magenta curves) for each excitation differs, with an estimated quantum yield of 56% for the 500 nm excitation data and 48% for the 575 nm excitation data. Overlap of excited-state and GS absorption bands hinders the absolute measurement of Φ, but the ratio of values for the two excitation wavelengths is very accurate, with 575 nm excitation producing 14% less Lumi-G_2. The SADS of both Lumi-G_1 and Lumi-G_2 have a photoproduct absorption whose magnitude is comparable to those of the bleach, SE and ESA bands of the ESI (Figure 8). Assuming that the chromophore extinction coefficient does not change excessively over the course of the photoreaction, an assumption we have shown to hold true for the forward reaction (DOI: 10.1021/bi201507k), our estimated absolute Φ of 48−56% is both reasonable and even higher than that observed in the forward reaction for NpR6012g4 [40% (DOI: 10.1021/bi201507k and ref 29)].

Figure 9 contrasts the SADS from the two data sets. The P_g* SADS (ESI, Figure 9A) differ in the bleach band, as expected.

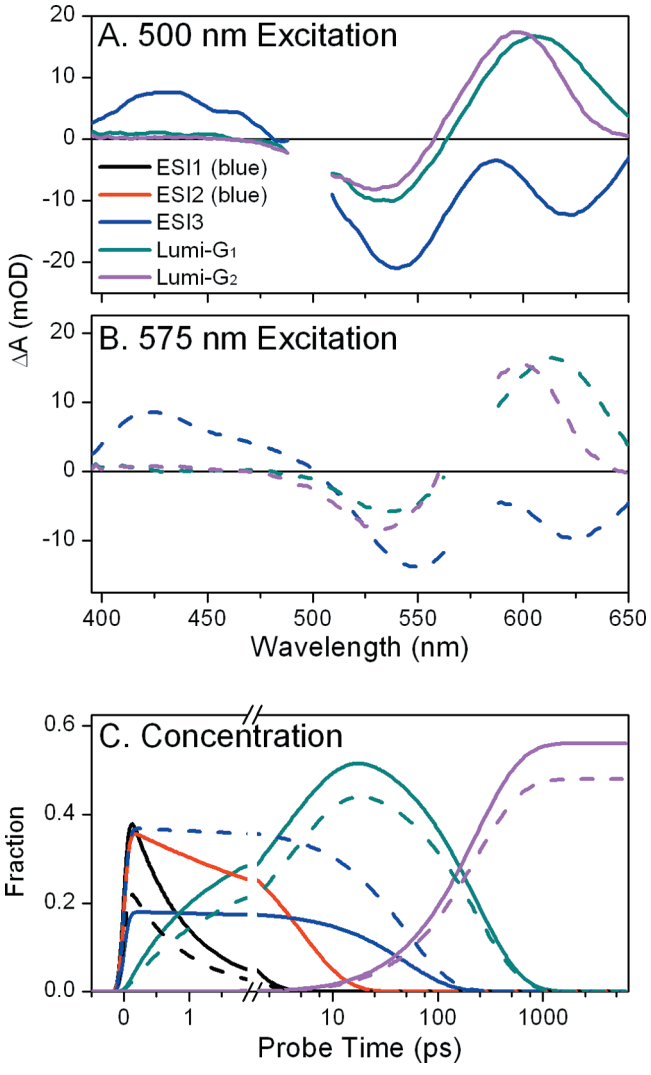

Figure 8. Spectra and compartmental flow from target analysis. SADS from the model described in Figure 7 are shown for 500 (A) and 575 nm (B) excitation. ESI1−ESI3 were constrained to have the same spectra in target analysis, so all are described by the blue line in panels A and B. (C) Concentration profiles of the spectral species are shown for the kinetic model in Figure 7, with comparison of 500 (solid lines) and 575 nm (dashed lines) excitation. The quantum yield for 500 nm excitation is 56% and that for 575 nm excitation data 48%.

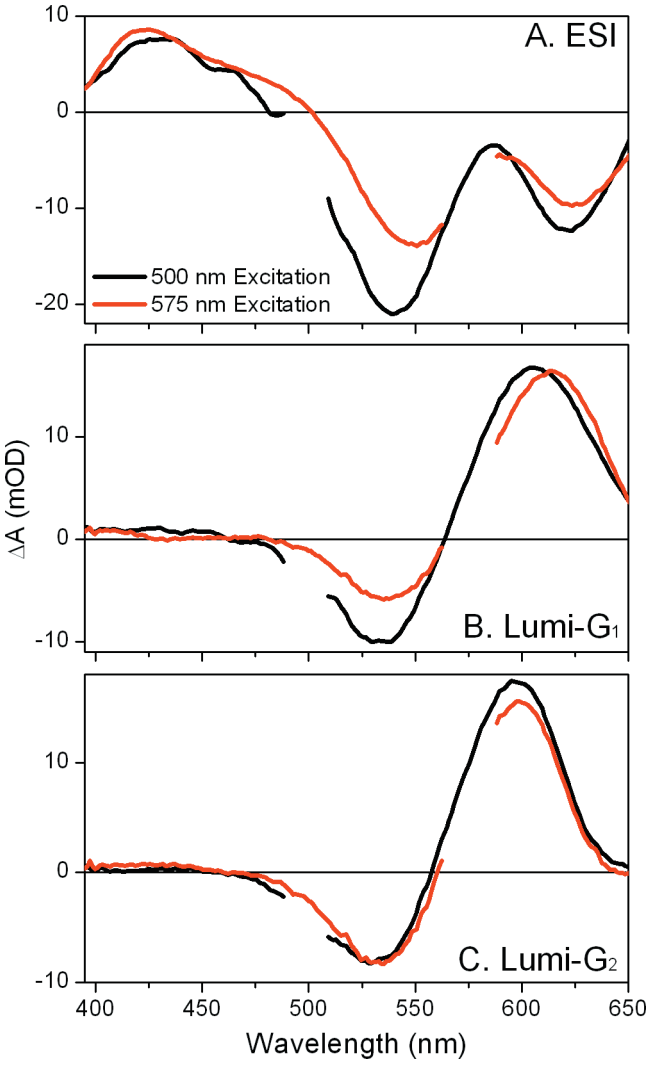

Figure 9. Comparison of SADS upon 500 (black) or 575 nm (red) excitation. SADS are compared without normalization for ESI (A), Lumi-G_1 (B), or Lumi-G_2 (C). Vertical lines indicate bleach minima, with the energy difference for those minima indicated in wavenumbers. No difference between minima was resolved in Lumi-G_2.

dx.doi.org/10.1021/bi2017365 | *Biochemistry* 2012, 51, 619−630

The bleach minimum for 500 nm excitation is 540 nm, and that for 575 nm excitation is 550 nm (340 cm^{-1} difference). Furthermore, the bleach amplitude is greater upon 500 nm excitation, while the amplitude of the 420 nm ESA band is comparable for both data sets. A similar trend is observed in the Lumi-G_1 SADS (Figure 9B), although the difference in bleach minima is smaller as expected. In contrast, the Lumi-G_2 SADS are nearly identical, with no wavelength-dependent amplitude or spectral shifts (Figure 9C). This is consistent with the sequential EADS analysis (Figure 5), suggesting that a ground-state equilibrium occurs between the initial GS populations on an ~200 ps time scale. Although the equilibration of initially distinct GS populations after selective excitation is evident from the data, this was not incorporated into the kinetic model during the fitting process. Thus, the SADS of the model (Figures 8 and 9) do not represent pure spectral populations in a manner independent of this equilibrium process, as is also indicated by differences in the bleach of corresponding SADS (ESI and Lumi-G_1 from Figure 9). The contribution of this equilibrium to the SADS is not sufficient to permit extraction of the underlying ground-state spectra, particularly in light of the lack of information about any equilibration of the non-productive GS3 that may occur. Even though it is not without limitations, the kinetic model accurately represents the primary reverse reaction photodynamics and provides useful spectral and kinetic information about the system.

DISCUSSION

NpR6012g4 is the first CBCR to be examined on the picosecond time scale; as such, it provides an interesting comparison to red/far-red phytochromes such as Cph1. Moreover, we have demonstrated surprisingly high quantum yields for photoconversion in this protein, raising the possibility of improving the quantum yield in other phytochromes and CBCRs by protein engineering. The interleaved pump−probe approach we employ here provides an unbiased mechanism of testing effects of excitation wavelength on photoproteins, while minimizing sample variation. Finally, our studies of NpR6012g4 also illustrate the extent to which the photoreceptors of the phytochrome superfamily are prone to heterogeneity. While we do not yet know the mechanism that tunes the absorbance of $^{15E}P_g$ to the green region of the spectrum, our demonstration of heterogeneity in this state will prove to be valuable in elucidating this mechanism.

Comparison to Red/Far-Red Phytochromes. We previously demonstrated that the excited-state kinetics for forward photoconversion of NpR6012g4 and Cph1 are comparable (DOI: 10.1021/bi201507k). Both NpR6012g4 and Cph1 convert from a 15*Z* red-absorbing ground state to a red-shifted Lumi-R photoproduct. Subsequent thermal evolution on the electronic ground-state surface results in formation of P_{fr} in Cph1 and $^{15E}P_g$ in NpR6012g4. In the reverse reaction studied here, the $^{15E}P_g$ ground state is distinct from P_{fr} in Cph1 as shown by their ground-state absorption spectra (Figure 10A). The P_g* and P_{fr}* excited-state spectra for these two proteins exhibit different ESA (420 and 510 nm peaks for NpR6012g4 and Cph1, respectively) and SE (630 and >700 nm, respectively) bands (Figure 10B), as expected on the basis of the different ground-state spectra (Figure 10A). However, a red-shifted primary photoproduct is formed in both reactions [Lumi-G_2 in NpR6012g4, and Lumi-F in Cph1 (Figure 10B)]. It is well established that the femtosecond dynamics of forming Lumi-F from P_{fr} in phytochromes are faster than the corresponding forward reaction of Lumi-R formation.[35,36,46,47] We here show that the same holds true for NpR6012g4, despite its strikingly different 15*E* ground state: the reverse dynamics are significantly faster than the forward dynamics. However, the reverse reaction for NpR6012g4 is still considerably slower than that of Cph1 (Figure 10C). The slower excited-state decay of NpR6012g4 relative to Cph1 is somewhat surprising in light of the much higher quantum yield observed with NpR6012g4 (see below), but it is in keeping with our observation of a higher quantum yield in the NpR6012g4 forward reaction than in the Cph1 forward reaction (DOI: 10.1021/bi201507k).

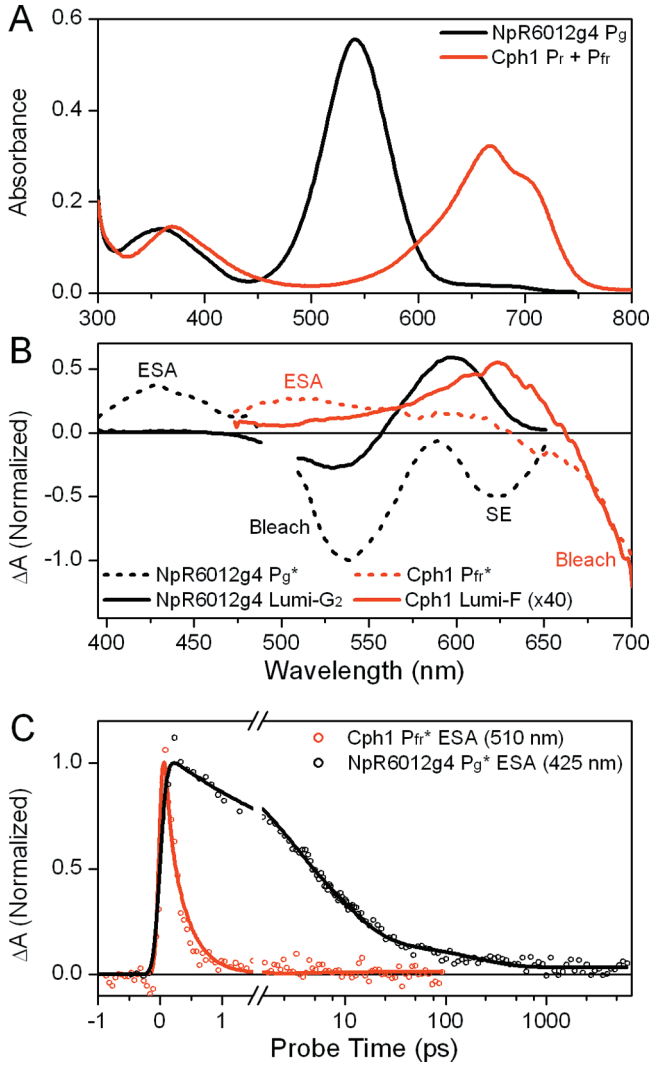

Figure 10. Comparison between the reverse reactions of NpR6012g4 (black) and Cph1 (red). (A) Ground-state absorbance spectra for NpR6012g4 in the $^{15E}P_g$ state and for Cph1 at the P_r−P_{fr} photoequilibrium. (B) Excited-state transient spectra (dashed lines) and primary photoproduct spectra (solid lines) are shown. Excited-state spectra were normalized at the ESA bands (420 and 500 nm for NpR6012g4 and Cph1, respectively), and the Cph1 primary photoproduct spectrum (Lumi-F) was magnified by a factor of 40 for comparison to that of NpR6012g4. ESA, SE, and bleach bands of P_g* and P_{fr}* are indicated for the sake of clarity. (C) Kinetic traces (circles) at the indicated wavelengths were normalized at the maxima and fitted with the global sequential model (lines).

We observed that the primary NpR6012g4 photoproduct Lumi-G_1 evolves on the ground-state surface within 1 ns of photoexcitation (Figure 3). This Lumi-G_1 → Lumi-G_2

dx.doi.org/10.1021/bi2017365 | *Biochemistry* 2012, 51, 619−630

transition occurs with a 230 ps time constant (Figure 7), with Lumi-G_2 exhibiting a blue-shifted and narrower absorption than Lumi-G_1 (Figure 8A,B). Such ground-state dynamics are not observed in the forward reactions of canonical phytochromes, in which the primary initial photoproduct Lumi-R decays in a microsecond range,[25,48] or of NpR6012g4 (DOI: 10.1021/bi201507k). However, complicated ground-state dynamics have been reported for the reverse reaction of P_{fr} systems. In P_{fr}, an extremely rapid (300−500 fs) excited-state decay is observed, followed by decay of the photoproduct with a relaxation time ranging from 3−4 to 400 ps.[35,36,49] The $^{15E}P_g$ state of NpR6012g4 has longer excited-state dynamics compared to the P_{fr} dynamics of canonical phytochromes,[35,36,46,49] with the faster productive population decaying in 800 fs and the slower productive population decaying in 5 ps (Figure 7 and Table 1). However, both reverse reactions exhibit evolution of the primary photoproduct on a subnanosecond time scale.

For the Lumi-G_1 → Lumi-G_2 transition of NpR6012g4, the narrowing of the absorption band indicates reduced freedom of motion for the chromophore in the binding pocket. A small blue shift indicates a minor thermal structural deformation of the chromophore concurrent with a fast rearrangement of the protein binding pocket that stabilizes the chromophore. Yang et al. proposed a multistep "flip-and-rotate" model from X-ray crystal structures,[13,50] whereupon the initial D-ring flip triggers a subsequent rotation of the chromophore in the plane of the B- and C-rings within the pocket. This model has been further supported by NMR studies by Matysik and co-workers[8,51,52] and by detailed temperature-scan cryocrystallography on a bacteriophytochrome where the subsequent relaxation events after the D-ring flip were observed.[53] The general trend in ground-state evolution suggested by these studies is the formation of stronger interactions between the chromophore and the binding pocket. Although there is not yet structural information for NpR6012g4, our observation of the evolution of Lumi-G_1 to Lumi-G_2 is consistent with such a model and hence raises the possibility that such a model will apply to both phytochromes and CBCRs.

Figure 11 presents a simplified potential energy surface (PES) diagram of the primary reverse reaction of NpR6012g4.

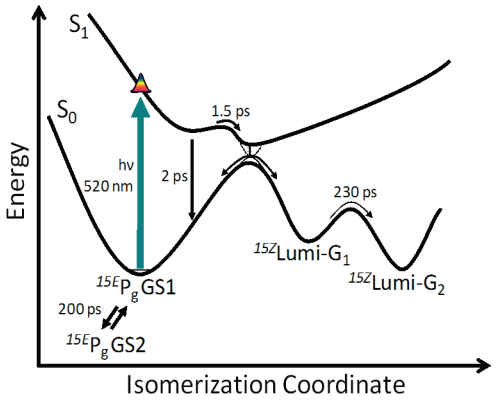

Figure 11. Potential energy surface diagram of the initial photodynamics of the NpR6012g4 reverse reaction along a one-dimensional reaction coordinate. Only the ^{15E}Pg GS1 potential energy surface is described; the indicated 200 ps equilibration between GS1 and GS2 implies a second, similar potential energy surface for photoreaction of GS2, but this has been omitted for the sake of clarity. The excited population encounters an excited-state barrier before quenching to the isomerized Lumi-G_1 ground state. The subsequent ground-state evolution of Lumi-G_1 forms Lumi-G_2 with a 230 ps time constant.

For the sake of simplicity, a full PES is shown only for GS1 (Figure 7), although that for GS2 should be broadly similar; nonproductive GS3 is not considered. We propose a potential energy barrier on the excited-state surface, the height of which varies depending on the GS population. Such a situation could arise because of the structural heterogeneity of the protein matrix around the chromophore: for example, different side chain rotamers of even a single critically positioned amino acid could modulate or even block progress on the excited-state surface but would be a property of the ground state, resulting in the observed heterogeneity. Such a residue could provide a simple steric blockade, or it could provide hydrogen bonds or $\pi-\pi$ interactions that alter the dynamics of the excited-state chromophore.[32,54] After passing this barrier, the excited-state population decays via a conical intersection. ESI1 and ESI2 generate Lumi-G_1 with time constants of 2 and 5 ps, respectively (Figure 7), while ESI3 does not generate Lumi-G_1. A more detailed mechanistic understanding will require atomic-resolution structural data and more spectroscopic data, such as time-resolved vibrational techniques.

Quantum Yield. The estimated Φ for the NpR6012g4 reverse reaction is remarkably high at 56 or 48% after 500 or 575 nm excitation, respectively (Figure 8C). In contrast, the Φ for P_{fr} to P_r photoconversion in Cph1 is estimated to be 16%.[55] Therefore, the slower decay of NpR6012g4 produces a higher quantum yield. This is surprising, because photoisomerization reactions exhibit a rough correlation between faster decay and higher Φ values. For example, rhodopsin exhibits exceptionally fast decay and a high Φ (τ = 200 fs; Φ = 70%), while PYP (τ = 2 ps; Φ = 33%) and the forward reaction of Cph1 ($P_r \rightarrow P_{fr}$; τ = 10 ps; Φ = 16%) are slower and less efficient.[36,56,57] Of course, there are exceptions to this trend; El-Sayed and coworkers showed for bacteriorhodopsin that a 20-fold variation in reaction rate did not affect quantum yield,[58] and the reverse reaction of Cph1 has an estimated Φ (~16%) comparable to that of the forward reaction despite much faster excited-state decay [~400 fs (Figure 10C)].[55] The reverse reaction for NpR6012g4 is also an exception, but in a different way: its excited-state dynamics are slower than in the Cph1 reverse reaction (Figure 10C), yet its Φ is 3−5-fold higher.[35,46,55]

Obtaining a model-independent quantification of Φ from ultrafast data can be difficult and requires the accurate measurement of both the population of initially excited chromophores and the population of the isomerized photoproduct. This can be done by careful examination of the ground-state bleach as a function of time if the bleach band does not have any interfering signals, as was the case for PYP.[37,59,60] However, the bleach bands of P_g* and Lumi-G_2 overlap both the negative SE signals at short times and the ESA and Lumi-G_2 positive absorption bands (Figure 3). The forward reaction of NpR6012g4 does not have a clean bleach band either, but in that case Φ was first estimated by comparison of the magnitude of the primary photoproduct absorption band with Cph1 signals assuming similar extinction values (DOI: 10.1021/bi201507k) and was subsequently confirmed by broadband pump−dump−probe techniques.[29] Unfortunately, comparison of Lumi-G in NpR6012g4 with Lumi-F in Cph1 is complicated by their very different spectral features (Figure 10B). Lumi-G_2 has a much higher absorption magnitude than Lumi-F in spectra normalized to the bleach amplitude and gives rise to strong signals both in the raw data (Figure 3) and in the SADS (Figure 8). Such a strong photoproduct signal indicates that either Φ for generating Lumi-G_2 in NpR6012g4 is significantly higher than that for generating Lumi-F in canonical phytochromes or the Lumi-G_2 extinction coefficient is significantly higher than the

dx.doi.org/10.1021/bi2017365 | *Biochemistry* 2012, 51, 619−630

Lumi-F extinction coefficient. While it is unlikely that the Lumi-G_2 extinction coefficient will be 3 times higher than that of Lumi-F, it will be necessary to use vibrational[34] or pump−dump−probe[29] spectroscopy to provide a better measurement of Φ.

Inhomogeneous Dynamics. A common feature of ultrafast spectroscopic studies of phytochrome systems and other photoactive proteins is the observation of multiphasic excited-state decay kinetics.[34−36,39,46,49,61−63] Such complex decay is often discussed either as arising from a homogeneous ground state with complex evolution on the excited-state surface[33−36,46,47,61] or as arising from simultaneous excitation of distinct ground-state subpopulations, each of which exhibits different excited-state kinetics.[32,63] Admixtures of homogeneous and inhomogeneous models can also be constructed,[61,64,65] but simple pump−probe data do not typically contain enough information to justify their use alone. All three approaches are capable of describing transient ultrafast signals, making it difficult to identify the correct model. Additional data, such as time-resolved vibrational spectra or pump−dump−probe results, can provide additional constraints to allow unambiguous interpretation.

In the case of the reverse reaction of NpR6012g4, it is indeed possible to fit our data to a model with a homogeneous ground state and complex excited-state evolution (Figures S4 and S5 of the Supporting Information). Hence, this is a case in which the presence of multiphasic excite-state kinetics alone is not definitive. However, the interleaved pump−probe approach we have used (Figure 3) provides additional constraints and justifies an inhomogeneous ground state. The interleaved PP signals reveal wavelength-dependent shifts in the ground-state bleach (Figure 3). Both homogeneous and inhomogeneous models are able to replicate this behavior (Figure 8 and Figure S4 of the Supporting Information); however, to do so, the homogeneous model predicts a different ground-state bleach depending on the excitation wavelength and hence might be viewed as implicitly containing ground-state heterogeneity. Moreover, the shift of the ground-state bleach is absent at later times (Figure 5), indicating that the bleached populations interconvert on a 200 ps time scale. A homogeneous description of the ground state cannot account for such ground-state equilibration, because it predicts no ground-state subpopulations exist. Taken together, these points make the homogeneous description problematic and justify description of $^{15E}P_g$ as a heterogeneous ground state.

Several spectroscopic and theoretical studies have suggested the existence of ground-state heterogeneity in phytochrome systems. Holzwarth et al. observed two distinct bleach bands at 720 and 740 nm in the P_{fr} dynamics of plant PhyA from oat,[35] suggesting a heterogeneous ground-state population. Static Raman spectra of the bacteriophytochromes DrBphP and Agp1 were also interpreted in terms of ground-state heterogeneity,[66] and this was supported by molecular dynamics simulations,[67] which found two energetically identical ground states for P_r, one of which was resolved in the crystal structure.[10] For Cph1, the situation is less clear. Both time-resolved Raman data and the static P_r absorbance spectrum have been interpreted as a homogeneous model.[34,68] Simulations supported a stable homogeneous PCB chromophore structure in the P_r state[69] and resolved in the crystal structure.[12] However, solid-state NMR work recently resolved two distinct P_r populations, one of which is found in the crystal structure[8] and the other of which has been described in hybrid quantum mechanics (QM)/molecular mechanics (MM) simulations.[70]

Concluding Comments. We have performed the first femtosecond study of the reverse reaction of a CBCR, NpR6012g4. In contrast to the forward reaction dynamics resolved in our earlier studies, the reverse dynamics exhibited faster excited-state and primary photoproduct formation dynamics. A novel interleaved PP approach was used to reveal and characterize a spectrally dynamic wavelength-dependent ground-state bleach, which is attributed to multiple ground-state subpopulations. The reaction exhibits a Φ of ∼50% that is also dependent on excitation wavelength and is significantly higher than that observed in canonical red/far-red phytochromes (∼15%). Further, the high Φ observed with NpR6012g4 raises the possibility of introducing higher quantum yields for other members of the phytochrome superfamily. In this regard, it is particularly interesting to note that the high Φ reported here for the reverse reaction does not require a productive ground-state intermediate, as was the case for the forward reaction.[29]

■ ASSOCIATED CONTENT

Ⓢ Supporting Information

Five figures. This material is available free of charge via the Internet at http://pubs.acs.org.

■ AUTHOR INFORMATION

Corresponding Author

*Department of Chemistry, University of California, Davis, CA 95616. Telephone: (530) 754-9075. E-mail: dlarsen@ucdavis.edu.

Funding

This work was supported by a grant from the Chemical Sciences, Geosciences, and Biosciences Division, Office of Basic Energy Sciences, Office of Science, U.S. Department of Energy (DOE DE-FG02-09ER16117), to J.C.L. and D.S.L.

■ ACKNOWLEDGMENTS

We thank Lu Zhao for help with data collection.

■ ABBREVIATIONS

CBCR, cyanobacteriochrome; CBD, chitin-binding domain; EADS, evolution-associated difference spectrum; SADS, species-associated difference spectra; ESI, excited-state intermediate; ESA, excited-state absorption; GAF, domain name derived from cGMP phosphodiesterase/adenylyl cyclase/FhlA; GSA, ground-state absorbance; NOPA, noncollinear optical parametric amplifier; PAS, domain name derived from Per-ARNT-Sim; PCB, phycocyanobilin; P_r, red-absorbing ground state of red/far-red phytochromes; P_{fr}, far-red-absorbing photoproduct state of red/far-red phytochromes; $^{15Z}P_r$, red-absorbing ground state of red/green CBCRs; $^{15E}P_g$, green-absorbing photoproduct state of red/green CBCRs; P_g*, excited-state population(s) derived from photoexcitation of $^{15E}P_g$; PYP, photoactive yellow protein; SE, stimulated emission; Φ, photocycle quantum yield

■ REFERENCES

(1) Rockwell, N. C., Su, Y. S., and Lagarias, J. C. (2006) Phytochrome structure and signaling mechanisms. *Annu. Rev. Plant Biol. 57*, 837−858.

(2) van der Horst, M. A., Key, J., and Hellingwerf, K. J. (2007) Photosensing in chemotrophic, non-phototrophic bacteria: Let there be light sensing too. *Trends Microbiol. 15*, 554−562.

(3) Hirose, Y., Narikawa, R., Katayama, M., and Ikeuchi, M. (2010) Cyanobacteriochrome CcaS regulates phycoerythrin accumulation in *Nostoc punctiforme*, a group II chromatic adapter. *Proc. Natl. Acad. Sci. U.S.A. 107*, 8854−8859.
(4) Möglich, A., Yang, X., Ayers, R. A., and Moffat, K. (2010) Structure and Function of Plant Photoreceptors. *Annu. Rev. Plant Biol. 61*, 21−47.
(5) Auldridge, M. E., and Forest, K. T. (2011) Bacterial phytochromes: More than meets the light. *Crit. Rev. Biochem. Mol. Biol. 46*, 67−88.
(6) Rockwell, N. C., and Lagarias, J. C. (2010) A Brief History of Phytochromes. *ChemPhysChem 11*, 1172−1180.
(7) Rohmer, T., Lang, C., Gartner, W., Hughes, J., and Matysik, J. (2010) Role of the Protein Cavity in Phytochrome Chromoprotein Assembly and Double-bond Isomerization: A Comparison with Model Compounds. *Photochem. Photobiol. 86*, 856−861.
(8) Song, C., Psakis, G., Lang, C., Mailliet, J., Gartner, W., Hughes, J., and Matysik, J. (2011) Two ground state isoforms and a chromophore D-ring photoflip triggering extensive intramolecular changes in a canonical phytochrome. *Proc. Natl. Acad. Sci. U.S.A. 108*, 3842−3847.
(9) Wagner, J. R., Brunzelle, J. S., Forest, K. T., and Vierstra, R. D. (2005) A light-sensing knot revealed by the structure of the chromophore-binding domain of phytochrome. *Nature 438*, 325−331.
(10) Wagner, J. R., Zhang, J. R., Brunzelle, J. S., Vierstra, R. D., and Forest, K. T. (2007) High resolution structure of *Deinococcus* bacteriophytochrome yields new insights into phytochrome architecture and evolution. *J. Biol. Chem. 282*, 12298−12309.
(11) Xiaojing, Y., Stojkovic, E. A., Kuk, J., and Moffat, K. (2007) Crystal structure of the chromophore binding domain of an unusual bacteriophytochrome, RpBphP3, reveals residues that modulate photoconversion. *Proc. Natl. Acad. Sci. U.S.A. 104*, 12571−12576.
(12) Essen, L. O., Mailliet, J., and Hughes, J. (2008) The structure of a complete phytochrome sensory module in the Pr ground state. *Proc. Natl. Acad. Sci. U.S.A. 105*, 14709−14714.
(13) Yang, X., Kuk, J., and Moffat, K. (2008) Crystal structure of *Pseudomonas aeruginosa* bacteriophytochrome: Photoconversion and signal transduction. *Proc. Natl. Acad. Sci. U.S.A. 105*, 14715−14720.
(14) Wu, S. H., and Lagarias, J. C. (2000) Defining the bilin lyase domain: Lessons from the extended phytochrome superfamily. *Biochemistry 39*, 13487−13495.
(15) Ikeuchi, M., and Ishizuka, T. (2008) Cyanobacteriochromes: A new superfamily of tetrapyrrole-binding photoreceptors in cyanobacteria. *Photochem. Photobiol. Sci. 7*, 1159−1167.
(16) Yoshihara, S., Katayama, M., Geng, X. X., and Ikeuchi, M. (2004) Cyanobacterial phytochrome-like PixJ1 holoprotein shows novel reversible photoconversion between blue- and green-absorbing forms. *Plant Cell Physiol. 45*, 1729−1737.
(17) Ishizuka, T., Shimada, T., Okajima, K., Yoshihara, S., Ochiai, Y., Katayama, M., and Ikeuchi, M. (2006) Characterization of cyanobacteriochrome TePixJ from a thermophilic cyanobacterium *Thermosynechococcus elongatus* strain BP-1. *Plant Cell Physiol. 47*, 1251−1261.
(18) Ishizuka, T., Narikawa, R., Kohchi, T., Katayama, M., and Ikeuchi, M. (2007) Cyanobacteriochrome TePixJ of *Thermosynechococcus elongatus* harbors phycoviolobilin as a chromophore. *Plant Cell Physiol. 48*, 1385−1390.
(19) Hirose, Y., Shimada, T., Narikawa, R., Katayama, M., and Ikeuchi, M. (2008) Cyanobacteriochrome CcaS is the green light receptor that induces the expression of phycobilisome linker protein. *Proc. Natl. Acad. Sci. U.S.A. 105*, 9528−9533.
(20) Narikawa, R., Fukushima, Y., Ishizuka, T., Itoh, S., and Ikeuchi, M. (2008) A novel photoactive GAF domain of cyanobacteriochrome AnPixJ that shows reversible green/red photoconversion. *J. Mol. Biol. 380*, 844−855.
(21) Rockwell, N. C., Njuguna, S. L., Roberts, L., Castillo, E., Parson, V. L., Dwojak, S., Lagarias, J. C., and Spiller, S. C. (2008) A second conserved GAF domain cysteine is required for the blue/green photoreversibility of cyanobacteriochrome Tlr0924 from *Thermosynechococcus elongatus*. *Biochemistry 47*, 7304−7316.
(22) Narikawa, R., Muraki, N., Shiba, T., Ikeuchi, M., and Kurisu, G. (2009) Crystallization and preliminary X-ray studies of the chromophore-binding domain of cyanobacteriochrome AnPixJ from *Anabaena* sp. PCC 7120. *Acta Crystallogr. F65*, 159−162.
(23) Ulijasz, A. T., Cornilescu, G., von Stetten, D., Cornilescu, C., Escobar, F. V., Zhang, J., Stankey, R. J., Rivera, M., Hildebrandt, P., and Vierstra, R. D. (2009) Cyanochromes Are Blue/Green Light Photoreversible Photoreceptors Defined by a Stable Double Cysteine Linkage to a Phycoviolobilin-type Chromophore. *J. Biol. Chem. 284*, 29757−29772.
(24) Zhang, J. A., Wu, X. J., Wang, Z. B., Chen, Y., Wang, X., Zhou, M., Scheer, H., and Zhao, K. H. (2010) Fused-Gene Approach to Photoswitchable and Fluorescent Biliproteins. *Angew. Chem., Int. Ed. 49*, 5456−5458.
(25) Fukushima, Y., Iwaki, M., Narikawa, R., Ikeuchi, M., Tomita, Y., and Itoh, S. (2011) Photoconversion Mechanism of a Green/Red Photosensory Cyanobacteriochrome AnPixJ: Time-Resolved Optical Spectroscopy and FTIR Analysis of the AnPixJ-GAF2 Domain. *Biochemistry 50*, 6328−6339.
(26) Ishizuka, T., Kamiya, A., Suzuki, H., Narikawa, R., Noguchi, T., Kohchi, T., Inomata, K., and Ikeuchi, M. (2011) The Cyanobacteriochrome, TePixJ, Isomerizes Its Own Chromophore by Converting Phycocyanobilin to Phycoviolobilin. *Biochemistry 50*, 953−961.
(27) Rockwell, N. C., Martin, S. S., Feoktistova, K., and Lagarias, J. C. (2011) Diverse two-cysteine photocycles in phytochromes and cyanobacteriochromes. *Proc. Natl. Acad. Sci. U.S.A. 108*, 11854−11859.
(28) Song, J. Y., Cho, H. S., Cho, J. I., Jeon, J. S., Lagarias, J. C., and Park, Y. I. (2011) Near-UV cyanobacteriochrome signaling system elicits negative phototaxis in the cyanobacterium *Synechocystis* sp. PCC 6803. *Proc. Natl. Acad. Sci. U.S.A. 108*, 10780−10785.
(29) KimP. W.FreerL. H.RockwellN. C.MartinS. S.LagariasJ. C.LarsenD. S. (2012)2012Second-Chance Initiation Dynamics of the Cyanobacterial Photocycle in the NpR6012 GAF 4 Domain of *Nostoc punctiforme*J. Am. Chem. Soc.
(30) van Stokkum, I. H. M., Larsen, D. S., and van Grondelle, R. (2004) Global and target analysis of time-resolved spectra. *Biochim. Biophys. Acta 1657*, 82−104.
(31) Holzwarth, A. R. (1996) Data Analysis of Time-Resolved Measurements. In *Biophysical techniques in photosynthesis* (Amesz, J., and Hoff, A. J., Eds.) pp 75−92, Springer, Dordrecht, The Netherlands.
(32) Toh, K. C., Stojkovic, E. A., van Stokkum, I. H. M., Moffat, K., and Kennis, J. T. M. (2010) Proton-transfer and hydrogen-bond interactions determine fluorescence quantum yield and photochemical efficiency of bacteriophytochrome. *Proc. Natl. Acad. Sci. U.S.A. 107*, 9170−9175.
(33) van Wilderen, L., Clark, I. P., Towrie, M., and van Thor, J. J. (2009) Mid-Infrared Picosecond Pump-Dump-Probe and Pump-Repump-Probe Experiments to Resolve a Ground-State Intermediate in Cyanobacterial Phytochrome Cph1. *J. Phys. Chem. B 113*, 16354−16364.
(34) Dasgupta, J., Frontiera, R. R., Taylor, K. C., Lagarias, J. C., and Mathies, R. A. (2009) Ultrafast excited-state isomerization in phytochrome revealed by femtosecond stimulated Raman spectroscopy. *Proc. Natl. Acad. Sci. U.S.A. 106*, 1784−1789.
(35) Müller, M. G., Lindner, I., Martin, I., Gartner, W., and Holzwarth, A. R. (2008) Femtosecond kinetics of photoconversion of the higher plant photoreceptor phytochrome carrying native and modified chromophores. *Biophys. J. 94*, 4370−4382.
(36) Heyne, K., Herbst, J., Stehlik, D., Esteban, B., Lamparter, T., Hughes, J., and Diller, R. (2002) Ultrafast dynamics of phytochrome from the cyanobacterium *Synechocystis*, reconstituted with phycocyanobilin and phycoerythrobilin. *Biophys. J. 82*, 1004−1016.
(37) Larsen, D. S., van Stokkum, I. H. M., Vengris, M., van der Horst, M. A., de Weerd, F. L., Hellingwerf, K. J., and van Grondelle, R. (2004) Incoherent manipulation of the photoactive yellow protein photocycle with dispersed pump-dump-probe spectroscopy. *Biophys. J. 87*, 1858−1872.

(38) Kennis, J. T. M., Larsen, D. S., van Stokkum, I. H. M., Vengris, M., van Thor, J. J., and van Grondelle, R. (2004) Uncovering the hidden ground state of green fluorescent protein. *Biophys. J. 86*, 168A.
(39) van Thor, J. J., Ronayne, K. L., and Towrie, M. (2007) Formation of the early photoproduct Lumi-R of cyanobacterial phytochrome Cph1 observed by ultrafast mid-infrared spectroscopy. *J. Am. Chem. Soc. 129*, 126−132.
(40) Larsen, D. S., Papagiannakis, E., van Stokkum, I. H. M., Vengris, M., Kennis, J. T. M., and van Grondelle, R. (2003) Excited state dynamics of β-carotene explored with dispersed multi-pulse transient absorption. *Chem. Phys. Lett. 381*, 733−742.
(41) Carroll, E. C., Compton, O. C., Madsen, D., Osterloh, F. E., and Larsen, D. S. (2008) Ultrafast carrier dynamics in exfoliated and functionalized calcium niobate nanosheets in water and methanol. *J. Phys. Chem. C 112*, 2394−2403.
(42) Toh, K. C., Stojkovic, E. A., van Stokkum, I. H. M., Moffat, K., and Kennis, J. T. M. (2011) Fluorescence quantum yield and photochemistry of bacteriophytochrome constructs. *Phys. Chem. Chem. Phys. 13*, 11985−11997.
(43) Takeuchi, S., and Tahara, T. (2004) Femtosecond absorption study of photodissociation of diphenylcyclopropenone in solution: Reaction dynamics and coherent nuclear motion. *J. Chem. Phys. 120*, 4768−4776.
(44) Lorenc, M., Ziolek, M., Naskrecki, R., Karolczak, J., Kubicki, J., and Maciejewski, A. (2002) Artifacts in femtosecond transient absorption spectroscopy. *Appl. Phys. B: Lasers Opt. 74*, 19−27.
(45) Kovalenko, S. A., Dobryakov, A. L., Ruthmann, J., and Ernsting, N. P. (1999) Femtosecond spectroscopy of condensed phases with chirped supercontinuum probing. *Phys. Rev. A 59*, 2369−2384.
(46) Schumann, C., Gross, R., Wolf, M. M. N., Diller, R., Michael, N., and Lamparter, T. (2008) Subpicosecond midinfrared spectroscopy of the P-fr reaction of phytochrome Agp1 from *Agrobacterium tumefaciens*. *Biophys. J. 94*, 3189−3197.
(47) Schumann, C., Gross, R., Michael, N., Lamparter, T., and Dilier, R. (2007) Sub-picosecond mid-infrared spectroscopy of phytochrome Agp1 from *Agrobacterium tumefaciens*. *ChemPhysChem 8*, 1657−1663.
(48) van Thor, J. J., Borucki, B., Crielaard, W., Otto, H., Lamparter, T., Hughes, J., Hellingwerf, K. J., and Heyn, M. P. (2001) Light-induced proton release and proton uptake reactions in the cyanobacterial phytochrome Cph1. *Biochemistry 40*, 11460−11471.
(49) Bischoff, M., Hermann, G., Rentsch, S., and Strehlow, D. (2001) First steps in the phytochrome phototransformation: A comparative femtosecond study on the forward (Pr → Pfr) and back reaction (Pfr → Pr). *Biochemistry 40*, 181−186.
(50) Yang, X. J., Kuk, J., and Moffat, K. (2009) Conformational differences between the Pfr and Pr states in *Pseudomonas aeruginosa* bacteriophytochrome. *Proc. Natl. Acad. Sci. U.S.A. 106*, 15639−15644.
(51) Rohmer, T., Lang, C., Bongards, C., Gupta, K., Neugebauer, J., Hughes, J., Gartner, W., and Matysik, J. (2010) Phytochrome as Molecular Machine: Revealing Chromophore Action during the Pfr → Pr Photoconversion by Magic-Angle Spinning NMR Spectroscopy. *J. Am. Chem. Soc. 132*, 9219 (Erratum).
(52) Rohmer, T., Lang, C., Hughes, J., Essen, L. O., Gartner, W., and Matysik, J. (2008) Light-induced chromophore activity and signal transduction in phytochromes observed by C-13 and N-15 magic-angle spinning NMR. *Proc. Natl. Acad. Sci. U.S.A. 105*, 15229−15234.
(53) Yang, X., Ren, Z., Kuk, J., and Moffat, K. (2011) Temperature-scan cryocrystallography reveals reaction intermediates in bacteriophytochrome. *Nature 479*, 428−U190.
(54) Fischer, A. J., and Lagarias, J. C. (2004) Harnessing phytochrome's glowing potential. *Proc. Natl. Acad. Sci. U.S.A. 101*, 17334−17339.
(55) Lamparter, T., Mittmann, F., Gartner, W., Borner, T., Hartmann, E., and Hughes, J. (1997) Characterization of recombinant phytochrome from the cyanobacterium *Synechocystis*. *Proc. Natl. Acad. Sci. U.S.A. 94*, 11792−11797.
(56) Kim, J. E., Tauber, M. J., and Mathies, R. A. (2001) Wavelength dependent cis-trans isomerization in vision. *Biochemistry 40*, 13774−13778.
(57) Vanbrederode, M. E., Gensch, T., Hoff, W. D., Hellingwerf, K. J., and Braslavsky, S. E. (1995) Photoinduced Volume Change and Energy-Storage Associated with the Early Transformations of the Phtoactive Yellow Protein from *Ectothiorhodospira halophila*. *Biophys. J. 68*, 1101−1109.
(58) Song, L., Elsayed, M. A., and Lanyi, J. K. (1993) Protein Catalysis of the Retinal Subpicosecond Photoisomerization in the Primary Process of Bacteriorhodopsin Photosynthesis. *Science 261*, 891−894.
(59) Carroll, E. C., Hospes, M., Valladares, C., Hellingwerf, K. J., and Larsen, D. S. (2011) Is the photoactive yellow protein a UV-B/blue light photoreceptor? *Photochem. Photobiol. Sci. 10*, 464−468.
(60) Carroll, E. C., Song, S.-H., Kumauchi, M., van Stokkum, I. H. M., Jailaubekov, A., Hoff, W. D., and Larsen, D. S. (2010) Subpicosecond Excited-State Proton Transfer Preceding Isomerization During the Photorecovery of Photoactive Yellow Protein. *J. Phys. Chem. Lett. 1*, 2793−2799.
(61) Holzwarth, A. R., Venuti, E., Braslavsky, S. E., and Schaffner, K. (1992) The Phototransformation Process in Phytochrome. 1. Ultrafast Fluorescence Component and Kinetic-Models for the Initial Pr → Pfr Transformation Steps in Native Phytochrome. *Biochim. Biophys. Acta 1140*, 59−68.
(62) Stamm, P., and Kumar, P. P. (2010) The phytohormone signal network regulating elongation growth during shade avoidance. *J. Exp. Bot. 61*, 2889−2903.
(63) Schmidt, P., Gensch, T., Remberg, A., Gartner, W., Braslavsky, S. E., and Schaffner, K. (1998) The complexity of the P-r to P-fr phototransformation kinetics is an intrinsic property of native phytochrome. *Photochem. Photobiol. 68*, 754−761.
(64) Papagiannakis, E., Vengris, M., Larsen, D. S., van Stokkum, I. H. M., Hiller, R. G., and van Grondelle, R. (2006) Use of ultrafast dispersed pump-dump-probe and pump-repump-probe spectroscopies to explore the light-induced dynamics of peridinin in solution. *J. Phys. Chem. B 110*, 512−521.
(65) Song, S.-H., Freddolino, P. L., Nash, A. I., Carroll, E. C., Schulten, K., Gardner, K. H., and Larsen, D. S. (2011) Modulating LOV Domain Photodynamics with a Residue Alteration outside the Chromophore Binding Site. *Biochemistry 50*, 2411−2423.
(66) von Stetten, D., Guenther, M., Scheerer, P., Murgida, D. H., Mroginski, M. A., Krauss, N., Lamparter, T., Zhang, J., Anstrom, D. M., Vierstra, R. D., Forest, K. T., and Hildebrandt, P. (2008) Chromophore heterogeneity and photoconversion in phytochrome crystals and solution studied by resonance Raman spectroscopy. *Angew. Chem., Int. Ed. 47*, 4753−4755.
(67) Kaminski, S., Daminelli, G., and Mroginski, M. A. (2009) Molecular Dynamics Simulations of the Chromophore Binding Site of *Deinococcus radiodurans* Bacteriophytochrome Using New Force Field Parameters for the Phytochromobilin Chromophore. *J. Phys. Chem. B 113*, 945−958.
(68) Spillane, K. M., Dasgupta, J., Lagarias, J. C., and Mathies, R. A. (2009) Homogeneity of Phytochrome Cph1 Vibronic Absorption Revealed by Resonance Raman Intensity Analysis. *J. Am. Chem. Soc. 131*, 13946−13948.
(69) Kaminski, S., and Mroginski, M. A. (2010) Molecular Dynamics of Phycocyanobilin Binding Bacteriophytochromes: A Detailed Study of Structural and Dynamic Properties. *J. Phys. Chem. B 114*, 16677−16686.
(70) Mroginski, M. A., von Stetten, D., Escobar, F. V., Strauss, H. M., Kaminski, S., Scheerer, P., Guenther, M., Murgida, D. H., Schmieder, P., Bongards, C., Gaertner, W., Mailliet, J., Hughes, J., Essen, L.-O., and Hildebrandt, P. (2009) Chromophore Structure of Cyanobacterial Phytochrome Cph1 in the Pr State: Reconciling Structural and Spectroscopic Data by QM/MM Calculations. *Biophys. J. 96*, 4153−4163.